Interaction between Ekman pumping and the centrifugal instability in Taylor–Couette flow

Olivier Czarny, Eric Serre, and Patrick Bontoux
LMSNM, FRE 2405 CNRS-Universités d'Aix-Marseille, IMT, La Jetée-Technopôle de Château-Gombert, 38 rue Frédéric Joliot-Curie, 13451 Marseille cedex 20, France

Richard M. Lueptow[a)]
Department of Mechanical Engineering, Northwestern University, Evanston, Illinois 60208

(Received 27 September 2002; accepted 7 November 2002; published 8 January 2003)

The endwalls in a Taylor–Couette cell introduce adjacent boundary layers that interact with the centrifugal instability. We investigate the interaction between the endwall Ekman layers and the Taylor vortices near transition from nonvortical to vortical flow via direct numerical simulation using a spectral method. We consider a radius ratio of $\eta=0.75$ in a short annulus having a length-to-gap ratio of $\Gamma=6$. To analyze the nature of the interaction between the vortices and the endwall layers, three endwall boundary conditions were considered: fixed endwalls, endwalls rotating with the inner cylinder, and stress-free endwalls. Below the critical Taylor number, endwall vortices for rotating endwalls are more than twice the strength of the vortices for fixed endwalls. This trend continues well above the transition to vortical flow, consistent with a simple force balance analysis near the endwalls. Stress-free endwalls result in endwall vortices that are similar in strength to those for rotating endwalls above the critical Taylor number. The endwall conditions significantly change the bifurcation diagram based on the radial velocity near the center of the annulus. For stress-free endwall conditions, the bifurcation is quite sharp, although only one fork of the bifurcation results unless the initial conditions are specifically set to favor the other fork. For rotating and fixed endwalls, there is a continuous transition from a featureless flow to a vortical flow due to the endwall vortices. © *2003 American Institute of Physics.* [DOI: 10.1063/1.1534108]

I. INTRODUCTION

The Taylor–Couette system of shear flow between a rotating inner cylinder and a concentric, fixed outer cylinder is a canonical system that provides valuable insight into the centrifugal stability of rotating flows as well as low-dimension bifurcation phenomena. Typically, the effects of the endwalls on the flow are avoided theoretically by assuming infinitely long cylinders, experimentally by using long cylinders (compared to the gap between the cylinders), and computationally by using periodic boundary conditions at the axial extrema of the computational domain. In this way, the centrifugal instability is considered without the interference of the confining endwalls. However, the endwalls are an important influence on the flow throughout the Taylor–Couette cell. Consequently, we consider the interaction between the boundary-driven flows at the endwalls and the centrifugal instability inherent in the Taylor–Couette configuration.

Away from the endwalls in cylindrical Couette flow, the stable flow is geostrophic. In other words, the centrifugal force due to the azimuthal velocity (or equivalently, the inertia related to the centripetal acceleration) is balanced by the pressure gradient force. No radial flow occurs when the Reynolds number is small enough so that viscosity suppresses the centrifugal (Taylor) instability. However, this geostrophic flow is upset at the endwalls where the no-slip boundary condition results in an azimuthal velocity near the endwall that is different from that far from the endwall. The imbalance between the pressure gradient force near the endwall, which is similar to the pressure gradient imposed by the flow far from the endwall, and the centrifugal force near the endwall, which is driven by the azimuthal velocity due to the rotation of the endwall, results in a force near the endwalls that drives a radial flow in a boundary layer on the endwalls. Depending on the nature of the endwall boundary condition, the boundary-driven flow at the endwall can be considered either a Bödewadt flow, where the endwall is fixed and the fluid is rotating, or an Ekman flow, where the endwall and fluid are rotating at different angular velocities. These endwall flows are part of the larger family of flows including Bödewadt, Ekman, and von Kármán (BEK) boundary layer flows.[1] For BEK flows, the thickness of the boundary layer scales with $(\nu/\Omega)^{1/2}$, where ν is the kinematic viscosity and Ω is an angular velocity scale.

The transition from stable cylindrical Couette flow to Taylor vortex flow is described by a pitchfork bifurcation when the cylinders are infinitely long to avoid endwall effects. However, the presence of the endwalls upsets the normal pitchfork bifurcation. This leads to one branch having a continuous transition from a featureless stable flow to a vortical flow with the rotation of the vortex adjacent to the endwall defined by the radial boundary flow. For fixed endwalls,

[a)]Author to whom correspondence should be addressed. Telephone: 847-491-4265; fax: 847-491-3915; electronic mail: r-lueptow@northwestern.edu

the rotation of the endwall vortex associated with the continuous branch is such that the flow adjacent to the endwalls is radially inward. For endwalls rotating with the inner cylinder, the rotation of the endwall vortices is such that the flow adjacent to the endwalls is outward. A second branch, which is disconnected from the first branch, corresponds to rotation of vortex near the endwall opposite that defined by the endwall boundary flow.[2] This second branch could be considered an ''anomalous'' branch, since the rotation of vortices near the endwall is opposite that normally expected based on the endwall boundary layer flow. In most cases, the flow follows the continuous branch, although it is possible to generate flows corresponding to the anomalous branch under certain conditions.[3,4]

The continuous transition from featureless flow to vortical flow along the continuous branch is quite evident both experimentally and computationally.[5–10] Below the critical Reynolds number for transition from nonvortical to vortical flow, a single vortex driven by the flow in the endwall boundary layer first appears near each endwall. These endwall vortices are often referred to as Ekman vortices.[6–8] The vortical structures are not an instability but instead are driven by the boundary layer flow at the endwalls. Because the equations of motion are elliptic, these endwall effects penetrate to some extent over the entire flow.[11]

As the Reynolds number is gradually increased, more vortices appear with a counter-rotating sense, such that the strength of the vortices decays exponentially with distance from the endwalls.[8] Although they are unrelated to the centrifugal instability of Taylor vortex flow, these counter-rotating vortices appear quite similar to Taylor vortices having an axial extent that is approximately equal to the gap between the cylinders. Once the transitional Reynolds number is reached, the vortex structure is driven by the Taylor centrifugal instability in addition to the boundary layer flow. Vortices fill the annulus, but the sense of rotation of the vortical structure is maintained so that the endwall vortices continue with the same sense as the original Ekman vortices. Thus, the endwall vortices that appear well below the transition to Taylor vortex flow excite the unstable Taylor vortices and subsequently determine the rotation of the entire vortex structure above the critical speed for the appearance of Taylor vortices, even for relatively long cylinders.[12] If the Reynolds number is impulsively increased from subcritical to supercritical instead of being increased gradually, the interface between the vortical motion near the endwalls and the stable flow propagates from the endwalls into the bulk of the annulus, eventually filling the annulus with vortices. From experimental and computational results, the time for the front to propagate one annular gap width is of the order $\tau = d^2/2\pi\nu$, where $d = r_o^* - r_i^*$ is the gap between cylinders of radius r_o^* and r_i^*.[8,13] [The viscous time scale τ can be derived from the characteristic time scale for spin-up of a fluid between a pair of rotating disks, $Ek^{-1/2}\Omega^{-1}$, where $Ek = \nu/\Omega L^2$ is the Ekman number, Ω is the rotational speed, and L is a typical length scale of the flow.[14] Using $L = d$ as the characteristic length scale, this spin-up time scale can be rewritten as the product of the viscous time scale and the time scale of rotation so that $Ek^{-1/2}\Omega^{-1} = (\tau T)^{1/2}$, where $T = 2\pi/\Omega$ is the period of rotation.]

Consequently, the endwalls play a significant role in the nature of the Taylor vortex flow. This is most easily evident for short cylinders, since the vortices are never far from the endwalls. For short cylinders, the transition to nonwavy vortical flow occurs at a slightly lower rotational speed,[15] presumably because of the perturbation by the endwall vortices. Furthermore, the subsequent transition to wavy vortical flow occurs at a higher rotational speed than in the case of infinitely long cylinders,[15] most likely because the endwall vortices related to the endwall boundary layers alter the vortical structure to minimize the tendency toward waviness. In addition, the distance between the endwalls can strongly influence the axial wave number. In the case of infinite cylinders, the azimuthal wave number is such that nearly square vortical cells occur. For aspect ratios that are even integers, the axial wavelength of the vortex pair is nearly that predicted by theory for identical endwall conditions. However, odd or noninteger aspect ratios results in vortices near the endwalls that stretch or compress to accommodate the proper vortical rotation required by the endwall conditions.[15] Anomalous vortex structures (along the disconnected branch of the bifurcation diagram) can be brought about most readily in short cylinders,[3,4,16] but can also occur for long cylinders upon impulsive startup.[17]

From the discussion above, it is clear that the flow in the endwall boundary layers in Taylor vortex flow strongly influences the centrifugal instability and the resulting flow field. This interaction is the topic of this paper. We consider the flow in a short Taylor–Couette cell to investigate how the endwall boundary layers interact with the vortical structures related to the Taylor centrifugal instability. By using fixed endwalls, endwalls rotating with the inner cylinder, and stress-free endwalls (modeling a free surface), we investigate how the interaction between the endwall boundary layer and the centrifugal Taylor instability affects the transition from nonvortical flow to steady, axisymmetric vortical flow and the nature of the final flow field.

II. A SIMPLE PREDICTION SCHEME FOR THE BOUNDARY LAYER FLOW

When the inner cylinder is rotating and the outer cylinder is stationary, the direction of the radial flow in the endwall layer is easy to predict. For endwalls rotating with the inner cylinder, centrifugal viscous pumping causes an outflow at the endwalls, which is similar to a von Kármán boundary layer for a disk rotating in an otherwise quiescent fluid. For endwalls fixed to the stationary outer cylinder, the imbalanced pressure gradient and centrifugal forces near the endwalls result in an inward flow, which is similar to a Bödewadt layer for a stationary disk and a rotating fluid.

The situation can be approached more quantitatively by considering a force balance on a cylindrical element that is $dz^* \times r^* d\theta \times dr^*$, or, equivalently, from considering the boundary layer approximation for the radial Navier–Stokes equation, which results in

$$-\frac{\partial p^*}{\partial r^*}+\frac{\partial \tau_{zr}^*}{\partial z^*}=-\rho\frac{v_\theta^{*2}}{r^*}, \tag{1}$$

where p^* is the pressure, τ_{zr}^* is the shear stress, ρ is the density, and $(v_r^*, v_\theta^*, v_z^*)$ are the velocities in the (r^*, θ, z^*) directions. In the geostrophic region, the gradient of the shear is zero, so the radial pressure gradient is balanced by the centrifugal force

$$\left.\frac{\partial p^*}{\partial r^*}\right|_{\text{geostrophic}}=\rho\frac{v_\theta^{*2}}{r^*}, \tag{2}$$

where $v_\theta^*(r^*)$ is the exact solution for cylindrical Couette flow. Thus, there is no force driving a radial flow (at least when the flow is centrifugally stable). Because of the no-slip condition at the endwall, the azimuthal velocity, v_θ^*, near the endwall is different from that away from the endwall. The azimuthal velocity very near the endwall can be approximated as $v_\theta^*=r^*\Omega_e$, where Ω_e is the angular velocity of the endwall. In addition, to a first approximation, the radial pressure gradient in the geostrophic portion of the flow is imposed on the fluid very near the endwall. This geostrophic pressure gradient can be found from the exact solution for cylindrical Couette flow based on Eq. (2). Using this and the estimate for the azimuthal velocity near the endwall in Eq. (1) results in

$$\frac{\partial \tau_{zr}^*}{\partial z^*}\approx\left.\frac{\partial p^*}{\partial r^*}\right|_{\text{geostrophic}}-\rho\Omega_e^2 r^*. \tag{3}$$

We specify an approximate equality here because the angular velocity of the fluid near the endwall is not exactly Ω_e, but only approaches this value. In addition, the geostrophic pressure gradient on the right side of the equation is only an estimate for the local pressure gradient based on the exact solution in Eq. (2) for stable cylindrical Couette flow far from the endwalls. Furthermore, the pressure gradient in vortical flow is modified by the presence of the endwall vortices. Nevertheless, Eq. (3) provides an estimate of the imbalance between the centrifugal force and the pressure gradient force, which drives the radial endwall flow. Of course, the viscous stress forming the left side of the equation, opposes motion of the fluid. As a result, when the right side of the equation is positive, the flow is inward at the endwall; when the right side of the equation is negative, the flow is outward at the endwall. This boundary layer flow at the endwalls determines the rotation of the vortices that appear near the endwall well below the critical speed for Taylor vortices, and, upon transition to unstable flow, the rotation of the vortices for the entire unstable flow field. However, we must note that due to the nonlinear nature of the flow, anomalous modes may exist having vortex rotation at the endwall opposite that predicted using this simple scheme.[11]

Equation (3) can also be used to predict the relative strength of the endwall vortices. For instance, Mullin and Blohm considered a situation with the inner cylinder rotating and the outer cylinder fixed for a cylinder length $(2h)$ to gap ratio of $\Gamma=2h/d=3$.[18] The upper endwall was fixed and the lower endwall rotated with the inner cylinder. Their computational and experimental results showed a much stronger vortex adjacent to the rotating endwall than near the fixed endwall. As they increased the rotational speed, the vortex nearest the rotating endwall grew larger, eventually eliminating the other vortices in the cell. Applying Eq. (3) to their geometry indicates that the maximum force driving the outward radial flow at the rotating endwall was more than twice as large as the maximum force driving the inward flow at the nonrotating endwall. Apparently, this effect was so strong that as the rotational speed was increased, the recirculating flow driven by the lower endwall boundary flow dominated the centrifugal instability resulting in a single vortex in the cavity.

Later in this paper, we use the estimate of the force imbalance near the endwall in Eq. (3) to aid in interpreting computational results for a wide range of endwall conditions. The advantage, of course, is that Eq. (3) allows the *a priori* prediction of the ''strength'' of the Ekman vortices as we ascertain the role of the endwall flow in its interaction with the centrifugal instability.

III. GEOMETRY AND NUMERICAL METHOD

The configuration that is considered is an annular cavity between two concentric cylinders of inner and outer radii r_i^* and r_o^*, with the inner cylinder rotating at Ω_i and the outer cylinder fixed. The flow is described by the incompressible Navier–Stokes equations written with cylindrical coordinates (r^*, z^*, θ) in an absolute frame of reference, according to the velocity-pressure formulation. Parameters characteristic of the physical problem are the Reynolds number $\mathrm{Re}=\Omega_i r_i^* d/\nu$, the radius ratio $\eta=r_i^*/r_o^*$, and the aspect ratio $\Gamma=2h/d$. The scales for the dimensionless variables of space, time and velocity are d or h, Ω_i^{-1}, and $\Omega_i r_i^*$, respectively. The dimensionless radial and axial coordinates are $r=(2r^*-r_o^*-r_i^*)/d$, $r\in[-1;1]$, and $z=z^*/h$, $z\in[-1;1]$ to allow the use of Chebyshev polynomials.

On the cylindrical boundaries, the dimensionless velocity (v_r, v_θ, v_z) obeys the no-slip condition

$$\begin{aligned} &v_r=v_z=0,\ v_\theta=1,\ \text{at}\ r=-1,\ z\in[-1;1],\\ &v_r=v_z=0,\ v_\theta=0,\ \text{at}\ r=1,\ z\in[-1;1]. \end{aligned} \tag{4}$$

Three endwall conditions are considered, depending on the angular velocity of the endwall, Ω_e: (1) Stationary endwall $(\Omega_e=0)$; (2) rotation of the endwall with the inner cylinder $(\Omega_e=\Omega_i)$; and (3) a stress-free boundary condition on the endwall (designated $\Omega_e=F$). In this last case, the free surface is assumed flat, and surface tension is neglected, so that the surface is a pure slip boundary. The boundary conditions on the endwalls are complicated by the difficulty in handling the singularity in the azimuthal velocity v_θ at the corner where the cylinder has a different rotational speed than the endwall. This occurs at $z=\pm1$ and: (1) $r=-1$ for $\Omega_e=0$; (2) $r=1$ for $\Omega_e=\Omega_i$. To handle this, the profiles at the upper and lower endwalls are set so that the velocity is that of the endwall except very near the singularity, where velocity exponentially changes to that of the adjacent cylinder. Thus, the dimensionless form of the boundary conditions for the azimuthal velocity at $z=\pm1$ are

$$v_r = v_z = 0, \quad v_\theta = \frac{e^{-ar} - e^{-a}}{e^{a} - e^{-a}}, \quad \text{for} \quad \Omega_e = 0,$$

$$v_r = v_z = 0, \quad v_\theta = \frac{(1-\eta)r + 1 + \eta}{2\eta} \cdot \frac{e^{-ar} - e^{-a}}{e^{a} - e^{-a}},$$

$$\text{for} \quad \Omega_e = \Omega_i, \tag{5}$$

$$v_z = 0, \quad \frac{\partial v_r}{\partial z} = \frac{\partial v_\theta}{\partial z} = 0, \quad \text{for} \quad \Omega_e = F.$$

The location of the region in which the velocity changes from that of the cylinder to that of the endwall depends on the sign of the decay coefficient a. The width of the region is set to about $0.05d$ by adjusting the magnitude of a. This small distance is consistent with the size of the gap between a rotating cylinder and an endwall rotating at a different speed that would be necessary in an equivalent experimental system.

Since we consider axisymmetric flows, the incompressible, dimensionless Navier–Stokes equations are solved with a two-dimensional version of the code used by Czarny *et al.*[19] This code uses a pseudo-spectral Chebyshev collocation method taking advantage of the orthogonality properties of Chebyshev polynomials and providing exponential convergence.[20] The time scheme is semi-implicit and second-order accurate. It is a combination of the second-order backward implicit Euler scheme for the time term, an explicit Adams–Bashforth scheme for the nonlinear terms, and an implicit formula for the viscous diffusion term.[21] An improved projection algorithm allows velocity-pressure coupling.[22] The mesh grid is defined by the Gauss–Lobatto collocation points along (r,z) with $N=61$ and $M=121$ being the number of points in the radial and axial directions for the spatial mesh. The high grid resolution in the axial direction is helpful in avoiding any predisposition to a particular number of vortices appearing due to a particular grid spacing.

Preliminary computations for a fixed outer cylinder ($\eta = 0.83$) were undertaken to compare our results to that expected for three aspect ratios: 16, 32, 48. In all cases Taylor vortices were obtained with the axial wavelength and critical Reynolds number ($\mathrm{Re}_{\mathrm{crit}}$) in good agreement with theory.[23]

Perhaps a more challenging test is to directly compare our numerical results with experimental results in a situation where the effect of endwalls is specifically addressed. Sobolik *et al.* measured the velocity gradients at the stationary outer wall using a three-segment electrodiffusion probe for $\Gamma = 9.85$ and $\eta = 0.9$ with fixed endwalls ($\Omega_e = 0$).[10] In this case, the critical Reynolds number for transition to vortical flow for infinitely long cylinders is $\mathrm{Re}_{\mathrm{crit}} = 138$.[23] Figure 1 shows a comparison of our axisymmetric computational results for one-half of the length of the annulus with the measurements for the case where $\varepsilon = \mathrm{Re}/\mathrm{Re}_{\mathrm{crit}} = 1.00$. The computations (bold curve) match the experimental results (data points[10]) fairly well, although the maxima in the computations are as much as 7% higher than the measurements. Nevertheless, the match can be considered quite good for two reasons. First, the precise value of the Reynolds number at which experimental data is obtained can usually only be estimated to within a few percent due to minor errors in measuring the viscosity, rotational speed, and diameter of the cylinders. In fact, Sobolik *et al.* indicate that their critical Reynolds number differed by as much as 3% from the theoretical value.[10] Changing the Reynolds number for the computations by only 1% to $\varepsilon = 0.99$ (shown as the fine curve in Fig. 1) brings the computations very close to the experimental results. Second, the electrodiffusion method has some inherent experimental error in it. Although Sobolik *et al.* do not provide an error analysis, their data for the directional characteristics of the probe suggest that an error of several percent would not be unreasonable. We have compared our computational results to their experiments at other Reynolds numbers, both above and below the critical Reynolds number, and find agreement similar to that shown in Fig. 1. Thus, we conclude that our computational results faithfully reproduce experimental results for a geometry that is very similar to those that we study.

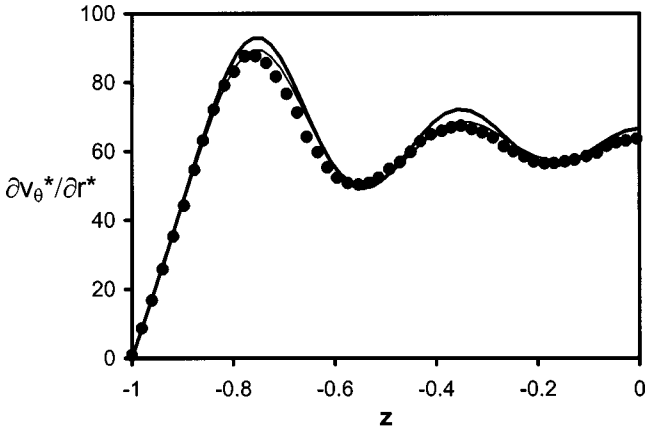

FIG. 1. Radial gradient of the azimuthal velocity: • experimental data at $\varepsilon = 1.00$; (Ref. 10) bold curve: computations at $\varepsilon = 1.00$; fine curve: computations at $\varepsilon = 0.99$.

IV. RESULTS

We consider the steady, axisymmetric flow near the transition from stable flow to vortical flow for an aspect ratio of $\Gamma = 6$ and a radius ratio of $\eta = 0.75$. The aspect ratio and radius ratio were chosen to match our previous computations for counter-rotating cylinders.[19] In addition, the small aspect ratio assures that the effect of the endwall condition is felt quickly near the midpoint of the length of the annulus. For infinitely long cylinders, the transition from nonvortical to vortical flow at this radius ratio occurs at $\mathrm{Re}_{\mathrm{crit}} = 85.8$.[23] We examine the character of the flow as the Reynolds number is varied from below this transition Reynolds number to well above it for all three endwall conditions. In all cases (such as that shown in Fig. 2), the velocity vectors in a meridional plane (v_r, v_z) at $r = 0$ (midway between the inner and outer cylinders) are plotted. The inner cylinder is the left vertical line, and the outer cylinder is the right vertical line. The vectors are scaled with $r_i^* \Omega_i$ at $\mathrm{Re}_{\mathrm{crit}}$ to permit comparison of the magnitudes of the velocities as the Reynolds number is increased and to evaluate the differences in the various endwall conditions.

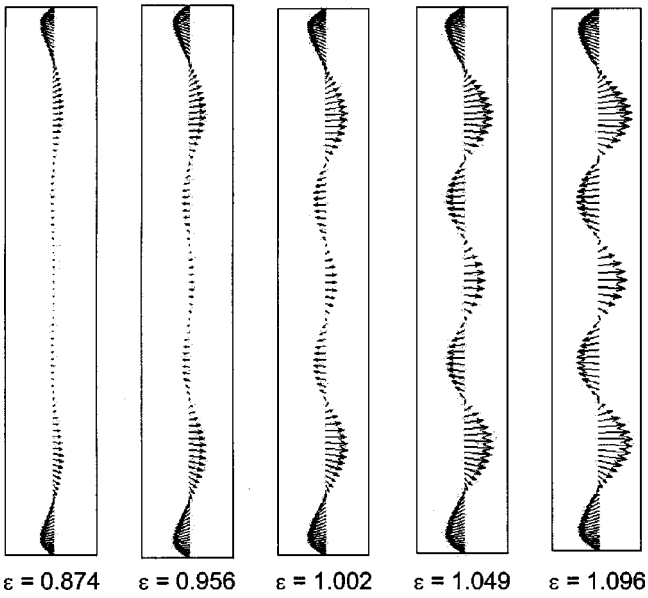

FIG. 2. Velocity vectors midway across the gap near transition from nonvortical to vortical flow for $\Gamma=6$, $\eta=0.75$, $\Omega_e=0$ (endwalls not rotating). The inner cylinder is the left vertical line; the outer cylinder is the right vertical line.

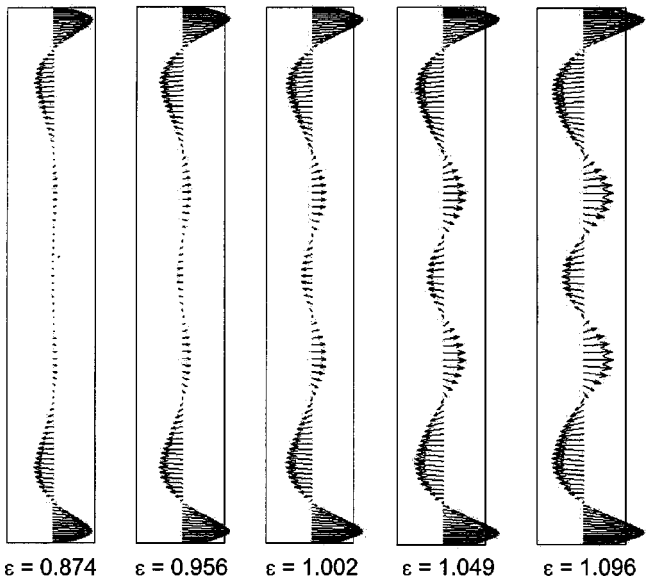

FIG. 3. Velocity vectors midway across the gap near transition from nonvortical to vortical flow for $\Gamma=6$, $\eta=0.75$, $\Omega_e=\Omega_i$ (endwalls rotating with the inner cylinder).

A. Fixed endwalls

Consider first the case of endwalls fixed ($\Omega_e=0$), shown in Fig. 2. Even well below the transition to Taylor vortex flow ($\varepsilon<1$), the inward flow at the endwalls induces a strong endwall vortex. The vortices near the center of the annular length are substantially weaker. As ε increases for $\varepsilon<1$, the endwall vortex remains nearly the same, but the vortices near the center grow in strength. All of the vortices for $\varepsilon<1$ are induced by the endwall boundary flow—they are not due to the centrifugal instability. As the Reynolds number is increased above the Reynolds number for transition ($\varepsilon>1$), the vortices near the center of the annulus continue to grow in strength, eventually growing somewhat stronger than the endwall vortex driven by boundary layer pumping for $\varepsilon>1.04$. On the other hand, it is interesting that the magnitude of the velocity in the endwall vortex just below the transition to vortical flow is similar to that for the Taylor vortices near the center of the annulus just above the transition, in spite of the very different mechanisms responsible for the appearance of the vortices. In both situations, the maximum radial velocity is about 3% to 4% of the surface speed of the inner cylinder. This suggests that while the mechanism that generates the vortices is quite different in the two cases, the geometry of the situation (most likely the gap width, d) and the inherent velocity scale in the problem ($r_i\Omega_i$) determine the magnitude of the velocity for the vortices.

The situation at the endwall vortex is quite interesting. One might expect that the velocity near the endwall might increase substantially at the transition from nonvortical to vortical flow due to the combined effect of the boundary-driven flow and the centrifugal instability. However, the vortex strength only continues to very gradually increase with ε around the transitional Reynolds number. This situation again suggests that the magnitude of the velocity in a vortex is determined by the inherent length and velocity scales for the situation, not the mechanism that causes the vortical motion.

The thickness of an endwall boundary layer should scale as $\delta_E/L\sim Ek^{1/2}=(\nu/\Omega L^2)^{1/2}$ according to the theory for Ekman layers.[14] Using the radii of one of the cylinders, r_i or r_o, or the gap width, d, for the length scale, L, provide similar results, so we choose to use d to be consistent with the length scale used for the spin-up time, discussed in the introduction. Based on this, one would predict an endwall boundary layer thickness of $0.19d$. The endwall boundary layer thickness can be estimated using the distance from the endwall to the position of the first maximum in the radial velocity midway across the gap. In the case of Fig. 2, δ_E ranges from $0.23d$ for $\varepsilon<1$ to $0.29d$ for $\varepsilon>1$, based on the computational grid location where the maximum radial velocity near the endwall occurs. Although these results seem somewhat high compared with the predicted value, the definition of the thickness of the endwall boundary layer is somewhat ambiguous in this case. We arbitrarily measured the thickness as the distance to the maximum radial velocity, but the thickness could have been defined in other ways. In addition, the vortical motion near the endwall clearly affects the thickness of the layer. For instance, the maximum radial velocity occurs at a much larger distance from the wall when measured nearer one of the cylinders rather than midway between them.

B. Rotating endwalls

Next, consider a similar sequence for the endwall rotating with the inner cylinder ($\Omega_e=\Omega_i$), shown in Fig. 3. The endwall flow is outward, which is opposite that for fixed endwalls, and is much stronger. This is a direct consequence of the force balance in Eq. (3). Figure 4 compares the theo-

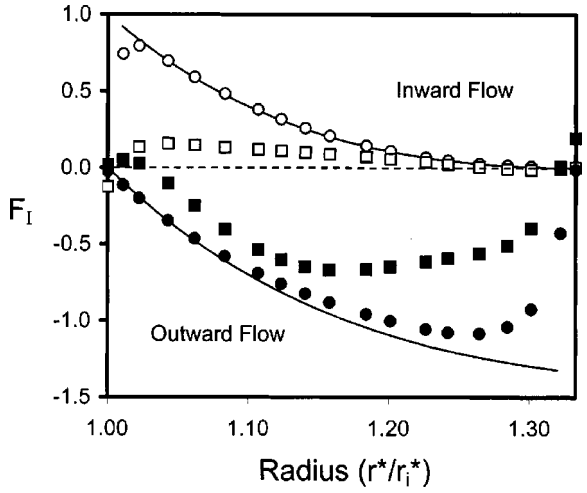

FIG. 4. Force imbalance near the endwall for $\Omega_e=0$ (open symbols) and $\Omega_e=\Omega_i$ (filled symbols). —— Eq. (3); circles are data based on pressure gradient at the center of the annulus; squares are data based on pressure gradient near the endwall.

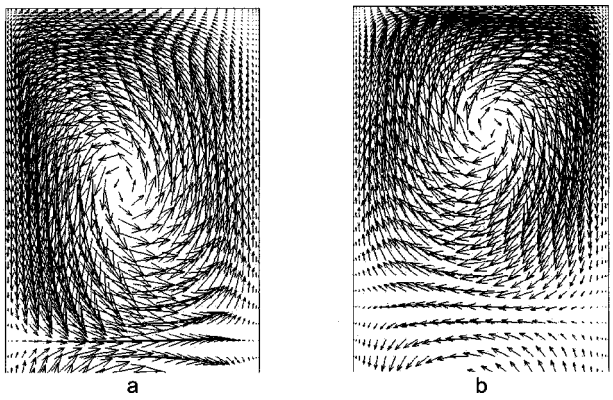

FIG. 5. Comparison of the velocity vectors near the upper endwall at $\varepsilon=0.98$ for (a) $\Omega_e=0$; and (b) $\Omega_e=\Omega_i$. Vectors are scaled identically in both cases. The inner cylinder is the left vertical line; the outer cylinder is the right vertical line.

retical and computed force imbalance, F_I, for both fixed and rotating endwalls as a function of radial position. [For the ordinate in Fig. 4, the left hand side of Eq. (3) is nondimensionalized so that force imbalance is $F_I=\partial\tau'_{zr}/\partial z'$, where $\tau'_{zr}=\tau^*_{zr}/\rho r_i^2\Omega_i^2$ and $z'=z^*/r_i^*$. This nondimensionalization scheme results in $0\leqslant F_I\leqslant 1$ for the case where the endwalls are fixed. However, data for the theoretical model are omitted at the inner or outer cylinders where singularities occur.] When $F_I>0$, the force imbalance generates an inward flow at the endwall; when $F_I<0$, the force imbalance generates an outward flow at the endwall. The force imbalance, F_I, is calculated just below transition to vortical flow at $\varepsilon=0.96$ in three ways for each case: (1) Using Eq. (3), which is based on the theoretical pressure gradient with no endwalls and the velocity of the endwall itself; (2) using the computed pressure gradient at the center of the gap ($z=0$), which is very similar to the theoretical pressure gradient with no endwalls, and the fluid's azimuthal velocity at computational grid locations very near the endwall ($z=0.991$, which is equivalent to $0.027d$ from the endwall); and (3) based on the computed pressure gradient and the fluid's azimuthal velocity, both at computational grid locations very near the endwall ($z=0.991$).

From Fig. 4, it is quite clear that no matter how the force imbalance is calculated, its magnitude is greater for the case of the endwall rotating with the inner cylinder than for a fixed endwall, thus explaining the stronger endwall layer flow when the endwall rotates with the inner cylinder. Of course, the direction of the endwall motion in Figs. 2 and 3 is also consistent with the prediction based on the force imbalance. The force imbalance calculated based on the radial pressure gradient at the center of the annulus and the azimuthal velocity near the endwalls is very similar to that predicted by Eq. (3). This is quite reasonable, given the assumptions in deriving Eq. (3) that the geostrophic pressure gradient (which is that far from the endwalls) is used in the calculation. However, when the force imbalance is calculated based on the local pressure gradient at computational grid locations very near the endwalls, its value is less than that predicted by Eq. (3). This is a consequence of the flow adjusting to the force imbalance by generating the radial endwall boundary flow. Nevertheless, the direction and relative magnitude of the endwall flow is consistent with the prediction of Eq. (3).

In spite of the stronger endwall vortices in the case of rotating endwalls, the vortical structure away from the endwalls is similar for both fixed and rotating endwalls, except for the sign of the velocity, as shown in Figs. 2 and 3. However, careful examination of the radial velocity at the axial midpoint of the domain shows that it is somewhat weaker for rotating endwalls than that for the case of fixed endwalls for $\varepsilon>1$. This is because the radial outflow is stronger than the radial inflow in Taylor vortex flow.[24–29] This effect is quite evident for the vortices away from the endwalls in both Figs. 2 and 3. Above transition, the radial outflow (rightward) is always stronger than the radial inflow except at the endwalls. In the case of fixed endwalls, the radial outflow coincides with the axial midpoint of the domain, so the radial flow at the midpoint is greater in this case. In addition, note that the flow is symmetric with respect to the midpoint of the annulus, as would be expected for an aspect ratio that is an even integer value. We note that the flow with rotating endwalls may become asymmetric for aspect ratios of 4 or less.[30]

Again the thickness of the endwall boundary layer can be determined based on the location of maximum radial velocity near the endwall. For rotating endwalls, δ_E is $0.15d$ both above and below the transition Reynolds number. Again, given the uncertainty in defining the endwall boundary layer thickness, this value is consistent with the predicted value of $0.19d$.

Returning now to the force imbalance indicated in Fig. 4, an interesting aspect is that the magnitude of the imbalance is greatest near the inner cylinder for fixed endwalls, and it is greatest near the outer cylinder for rotating endwalls. This suggests that the boundary layer flow might be stronger near the inner cylinder for fixed endwalls and near the outer cylinder first for rotating endwalls. This is indeed the case as is evident in Fig. 5, which depicts the velocity vectors for the boundary-driven vortex for $\varepsilon=0.98$ in both

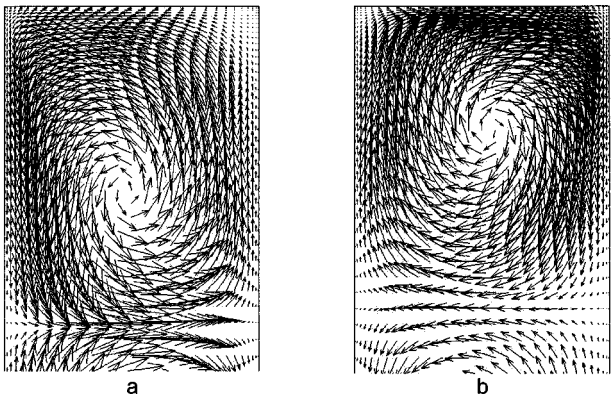

FIG. 6. Comparison of the velocity vectors near the upper endwall at $\varepsilon = 1.05$ for (a) $\Omega_e = 0$; and (b) $\Omega_e = \Omega_i$. Vectors are scaled identically in both cases.

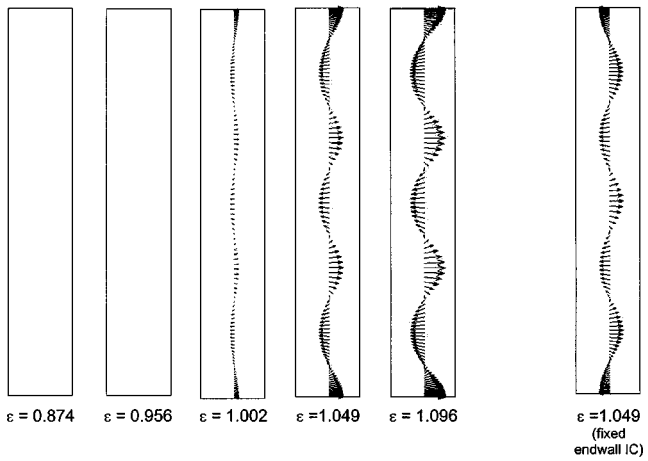

FIG. 7. Velocity vectors midway across the gap near transition for $\Gamma = 6$, $\eta = 0.75$, $\Omega_e = F$ (stress-free at the endwalls). The far right image shows the flow when the initial condition is fixed endwalls instead of quiescent flow.

cases. For the case of fixed endwalls, the strongest radial motion near the endwall is closer to the inner cylinder, as shown in Fig. 5(a). The strong inward radial flow near the inner cylinder leads to a very strong axial flow downward along the inner cylinder compared to the upward flow along the outer cylinder. This results in an asymmetric vortex with its center offset from the midpoint of the annular gap. In addition, the endwall vortex is somewhat elongated axially so that it does not have the square aspect ratio like that for a Taylor vortex, consistent with previous work.[5,9,10] The length of the endwall vortex is $1.30d$. In the case of rotating endwalls, the strongest radial flow at the endwall is nearer the outer cylinder, as shown in Fig. 5(b). The consequence is a strong downward axial flow at the outer cylinder, just the opposite of what occurs for fixed endwalls but still resulting in an asymmetric vortex. In this case, the vortex is elongated in the axial direction, but not as much as for the case of fixed endwalls—the length of the vortex is only $1.17d$. The reason for the difference in the elongation of the endwall vortices is not clear. It may simply be related to the stronger driving force for the rotating endwall generating a stronger vortex that is more compact.

Above the transition to Taylor vortex flow at $\varepsilon = 1.05$, the situation near the endwall is similar, as shown in Fig. 6 for both endwall conditions, even though the centrifugal instability in addition to the endwall boundary flow drives the vortex. One might expect that the Taylor centrifugal instability at this supercritical Reynolds number might cause the vortex to ''even out'' to a nearly uniform cell, but it does not do so for either endwall case. Apparently, the endwall boundary layer continues to drive a strong enough endwall flow to continue to affect symmetry of the endwall vortex structure. However, the endwall vortex for fixed endwalls has a slightly reduced axial extent of $1.27d$. The axial extent of the endwall vortices remains at $1.17d$ for rotating endwalls. The vortex centers are still offset from the midpoint of the annular gap. For the fixed endwall condition, the vortex center (estimated from the location where the radial and axial velocities appear to vanish) is $0.47d$ from the inner cylinder, whereas for the rotating endwall the vortex center is at $0.53d$ from the inner cylinder.

C. Stress-free endwalls

Although it is challenging to achieve experimentally, the case of stress-free boundary conditions at both endwalls can be readily modeled computationally. The appearance of the flow, as shown in Fig. 7, is quite different from the previous cases with the no-slip condition at the endwalls. The vortices do not appear at all below the critical Reynolds number. When the vortices first appear at $\varepsilon = 1$, they are nearly uniform in their strength along the length of the annulus. The flow near the stress-free endwall is nearly identical to that at the other vortices in terms of its amplitude, with the highest velocity right at the endwall. The radial velocity at the outflow boundaries between vortices increases more quickly with increasing ε than the velocity at the inflow boundaries. To accommodate this, the width of the outflow region decreases slightly, while the width of the inflow regions increases correspondingly.

The endwall vortex in this case is quite different from cases for which there is a no-slip boundary condition at the endwall, as shown in Fig. 8 in comparison with Fig. 6. In fact, the appearance of the vortex is very similar to that of a Taylor vortex away from an endwall boundary. With a stress-free endwall condition, the axial flow along the inner and outer cylinder walls is nearly the same. In addition, the endwall vortex is not axially elongated as with the vortices driven by either no-slip endwall condition. The axial length of the endwall vortex is $0.99d$, resulting in a square vortical cell like that for a Taylor vortex with the vortex center approximately midway between the inner and outer cylinders at $0.49d$ from the inner cylinder.

The computations for stress-free endwalls converged to an outflow at the endwalls beginning from a quiescent flow initial condition. However, we were able to obtain a solution with an inflow at the stress-free endwalls at a particular value of ε by using the solution for fixed endwalls at that ε as the initial condition. An example is shown in Fig. 7 for $\varepsilon = 1.049$. The flow is similar to that obtained at the same Reynolds number with stress-free endwall conditions, except that vortices are shifted by d and the velocity at the endwall

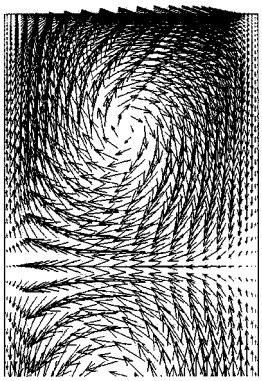

FIG. 8. Velocity vectors near the endwall at $\varepsilon = 1.05$ for $\Omega_e = F$. Vectors are scaled identically with those in Figs. 5 and 6.

is slightly smaller. This clearly shows how the initial conditions determine the final state. The nature of the convergence for the case of stress-free endwalls is also quite different from the other two cases. The flow takes about 100 times longer to computationally develop and converge for the stress-free endwall condition than for the no-slip endwall condition. This result amplifies how important the endwall vortices are as precursors to Taylor vortex flow.

The final case that we consider is that for a mixed endwall condition having a stress-free upper endwall and a rotating lower endwall, shown in Fig. 9. The development of the flow near the upper stress-free boundary is very similar to that for a stress-free boundary at both endwalls, shown in Fig. 7. Likewise, the development of the flow near the rotating lower boundary is very similar to that for a rotating boundary at both endwalls, shown in Fig. 3. The penetration of the vortices from the lower endwall into the annulus below the critical Reynolds number is quite clear. Below the

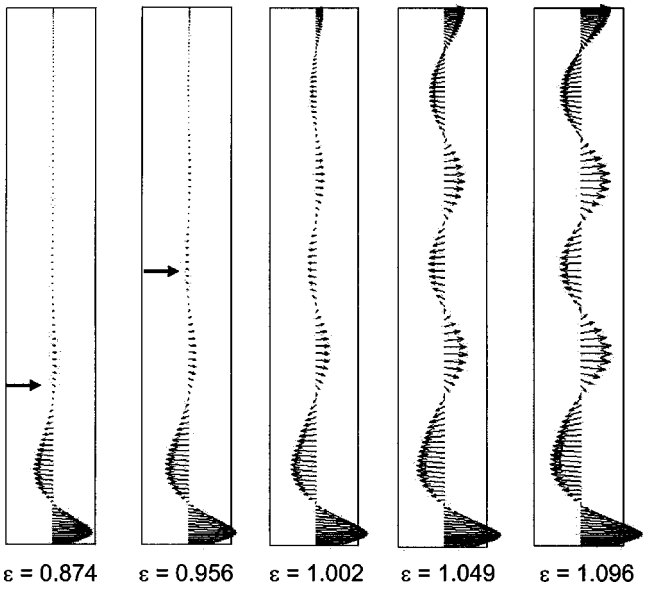

FIG. 9. Velocity vectors midway across the gap near transition from non-vortical to vortical flow for $\Gamma = 6$, $\eta = 0.75$, $\Omega_e = F$ at the upper endwall and $\Omega_e = \Omega_i$ at the lower endwall. Arrows mark the predicted penetration depth according to Eq. (6).

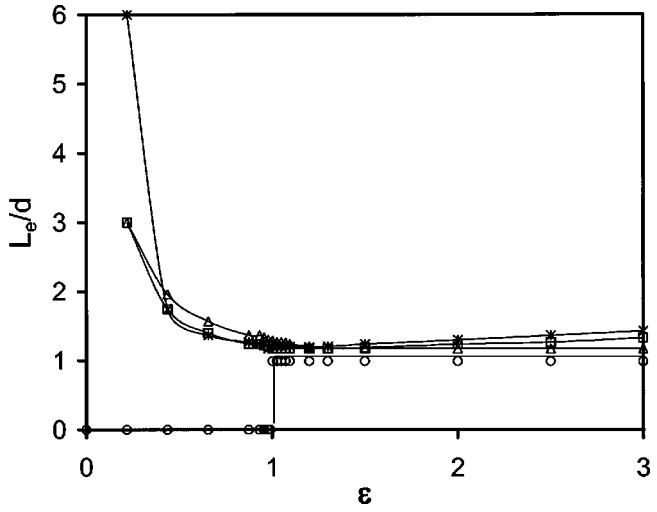

FIG. 10. Dependence of the length of the endwall vortex on the Reynolds number, $\varepsilon = \mathrm{Re}/\mathrm{Re}_{\mathrm{crit}}$, $\triangle$ $\Omega_e = 0$; $\square$, $\Omega_e = \Omega_i$; $\bigcirc$, $\Omega_e = F$ both endwalls; *, value at rotating endwall for mixed endwall conditions.

transition to vortical flow, the penetration depth, D, of endwall vortices from the endwall into the bulk of the annulus is given by[8]

$$D \approx 0.65|\varepsilon - 1|^{-1/2} d. \tag{6}$$

Using this relation, the estimated penetration depth is $1.8d$ and $3.1d$ for $\varepsilon = 0.874$ and 0.956. These locations, which are marked on Fig. 9, are consistent with our computational results.

V. DISCUSSION

It is clear from the results so far that the axial length of the endwall vortex depends on both the Reynolds number and the nature of the endwall boundary condition. Figure 10 displays the endwall vortex length, L_e, estimated from vector plots like those shown in Figs. 5, 6, and 8. Of course, the measurement of the length of the endwall vortex somewhat subjective, because the velocity is only available at discrete grid locations and the precise boundary between vortices is not always clearly defined. At low ε, the endwall vortices fill the length of the annulus, so that there are two vortices for the symmetric no-slip endwall conditions ($L_e/d = 3$) and a single large vortex for the mixed endwall condition ($L_e/d = 6$). As ε increases, more vortices appear in the annulus, reducing the length of the endwall vortex. At the transition Reynolds number, $\varepsilon = 1$, vortices of length $L_e/d = 0.99$ appear for the stress-free endwall condition, and the endwall vortex length has been reduced to $1.17 \leqslant L_e/d \leqslant 1.29$ for the cases of no-slip endwalls. With increasing ε, the endwall vortex length remains at $L_e/d = 0.99$ for the stress-free endwall condition and asymptotes to $L_e/d = 1.17$ for the fixed endwall case ($\Omega_e = 0$). However in the case of the endwalls rotating, either both endwalls or for the mixed endwall condition, the length of the endwall vortex increases slightly with increasing ε. The origin of this increase in size is not clear, although it may be related to the flow of energy into the endwall vortex due to the endwall rotation. However, because the aspect ratio, Γ, is an even integer, this last result

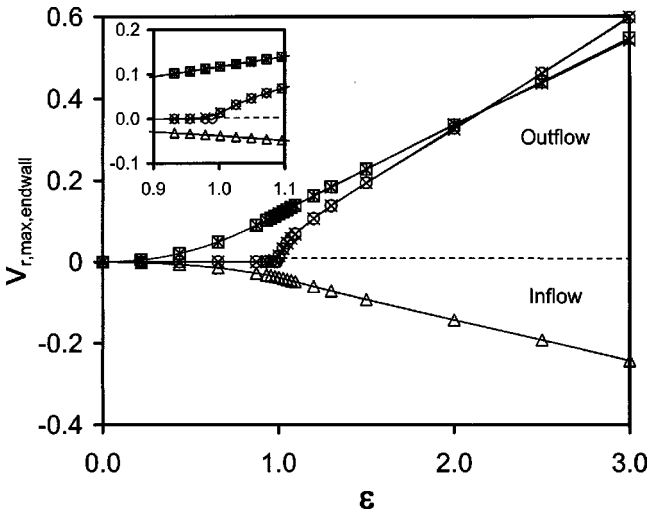

FIG. 11. Reynolds number dependence of the maximum radial velocity component nondimensionalized with $\Omega_i r_i^*$ near the endwall and midway across the annular gap. Inset shows the curves near transition. △, $\Omega_e=0$; □, $\Omega_e=\Omega_i$; ○, $\Omega_e=F$ both endwalls; ×, value at stress-free endwall for mixed endwall conditions; *, value at rotating endwall for mixed endwall conditions.

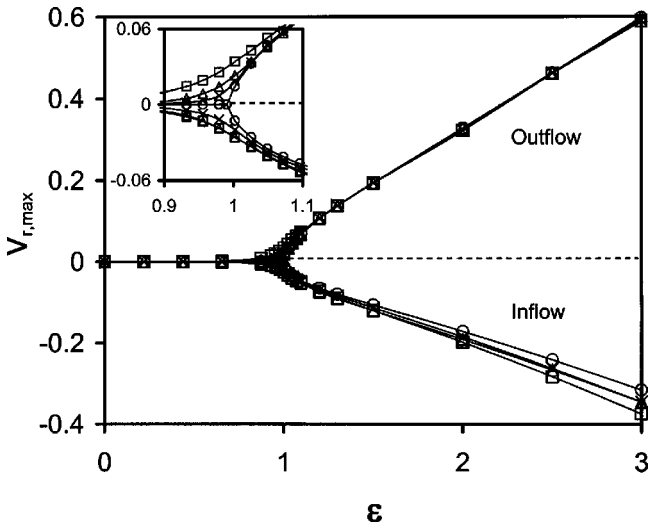

FIG. 12. Bifurcation diagram based on the maximum radial velocity nondimensionalized with $\Omega_i r_i^*$ at outflow regions and inflow regions near the axial center of the annulus. △, $\Omega_e=0$; □, $\Omega_e=\Omega_i$; ○, $\Omega_e=F$ both endwalls; ×, mixed endwall conditions.

indicates that the Taylor vortices away from the endwalls are somewhat reduced in size at the expense of the endwall vortices when $L_e/d \geqslant 1$, similar to the results with a larger aspect ratio.[5,9,31]

At this point, it is useful to examine the dependence of the radial velocity in the endwall layer, which is a measure of the strength of the endwall boundary layer, on the Reynolds number and endwall condition. The maximum radial velocity near the endwall halfway across the annular gap normalized by $r_i\Omega_i$ is shown in Fig. 11 for all of the endwall conditions that have been considered, including the values for the maximum radial velocity at each of the two endwalls for the mixed endwall case. (Note that since the vortex is not necessarily centered in the annular gap as shown in Figs. 5 and 6, the radial velocity may have a somewhat larger value at radial locations other than the center of the gap. Nevertheless, the maximum radial velocity at the center of the gap is used here to provide a consistent measure of the radial velocity in the endwall boundary layer.) For the cases in which the no-slip condition is imposed on the flow, the endwall velocity changes smoothly as the Reynolds number increases. Even at the transition to Taylor vortex flow at $\varepsilon=1$, the curve is quite smooth with no hint of a change in slope. The magnitude of the maximum radial velocity is larger for rotating endwalls than for fixed endwalls, since the driving force is larger, as was shown in Fig. 4.

One branch of the pitchfork bifurcation that is expected for stress-free endwalls is evident at $\varepsilon=1$. In this case, the transition from nonvortical flow to vortical flow results in a sharp increase in the radial velocity near the endwall. The lower branch of the bifurcation is not plotted in this figure because our simulations converged to the solution for a radial outflow at the stress-free endwall. A radial inflow at the stress-free endwall could be obtained only if the simulation was run with a fixed endwall result (having an inward flow at the endwall) as the initial condition. For the mixed endwall condition, the velocity near the stress-free endwall follows the curve for both endwalls being stress-free, while the velocity near the rotating endwall follows the curve for both endwalls rotating. In other words, even with a small aspect ratio of $\Gamma=6$, the influence of the rotating endwall is minimal at the stress-free endwall. The only exception occurs very near the transition to vortical flow at $\varepsilon=1$, where the velocity near the stress-free endwall in the mixed condition does not reflect as sharp of a change as that for both endwalls being stress-free, as shown in the inset of Fig. 11. It is also interesting to note that as ε increases, the maximum radial velocity near the stress-free endwalls becomes larger than that for the rotating endwalls, though not until the Reynolds number is well above the transition, $\varepsilon>2$. On the other hand, the magnitude of the maximum radial velocity for the fixed endwall case remains about one-half that of the stress-free or rotating endwalls. These results suggest that the friction near the endwalls reduces the energy of the vortical structures. This is a stronger influence in the case of fixed endwalls, where the endwall friction reduces the azimuthal momentum substantially more than in the case of rotating endwalls.

From the results presented so far, it is clear that the endwall conditions affect the nature of the bifurcation at the transition from nonvortical to vortical flow. We can further examine the bifurcation by considering the maximum radial velocity near the center of the axial length of the annulus as a function of ε, as shown in Fig. 12. The maximum radial velocity is recorded either at the midpoint of the axial length of the cylinders ($z=0$), or at the next inflow or outflow boundary above or below it. This was done so that the radial velocity at outflow boundaries and at inflow boundaries could be compared to one another. Depending on the endwall boundary conditions, the inflow and outflow boundaries occur either at the midpoint of the axial length or approximately d above or below the midpoint. For the mixed endwall condition, the asymmetry in the vortex field requires

that the local maximum value be measured at a slight axial offset from the center of the length of the annulus.

Considering first the inset in Fig. 12, it is clear that except for the case of both endwalls being stress-free, the endwall vortices reduce the sharpness of the bifurcation, consistent with previous results.[9,32] From the entire range of ε, it is clear that above the transition to vortical flow, the radial velocity at the inflow boundaries is only about 60% of the magnitude of the radial velocity at the outflow boundaries. It is interesting that the radial velocity at outflow boundaries collapse onto a single curve, regardless of the endwall condition. However, for inflow boundaries, the radial velocity for the stress-free endwall condition is slightly smaller than that for no-slip endwall conditions. Furthermore, this result is opposite that evident in Fig. 11 in which the stress-free condition results in the highest radial velocity near the endwall at high ε. The reason for this is not clear, although it may be related to differences in the size of the vortices. For stress-free endwalls, the vortices have an axial extent of about d, whereas for no-slip endwalls the vortices near the center are smaller because of the large endwall vortices. Since the outflow velocity is similar for all endwall conditions, it is reasonable to assume that the outflow region has a similar width in the axial direction in all cases. Consequently, the inflow region for no-slip endwalls must be narrower than the inflow region for stress-free conditions because of the smaller vortices for the no-slip endwalls. The result is a narrower inflow region for no-slip endwalls, which will then result in a slightly greater inflow velocity.

VI. CONCLUSIONS

The problem of endwalls boundary layers and their interaction with the centrifugal instability in Taylor–Couette flow has been frequently noted, but rarely directly addressed in the literature. Notable exceptions include the work on anomalous vortices and bifurcation phenomena by Benjamin, Mullin, and co-workers,[2–4,11,18,30,32,33] the analysis of vortex front propagation from an endwall by Ahlers, Lücke, and co-workers,[7,8] and the experiments of Sobolik *et al.*[10] In this paper, we focus on somewhat different aspects of the problem: The effect of the endwall condition on the nature of the interaction of the endwall vortices with the centrifugal instability, the implications of the interaction between endwall vortices and Taylor vortices on the structure of the velocity field near the endwalls, and the net effect of the endwall conditions on the bifurcation phenomena.

The endwall vortex strength is greatly affected by the type of endwall boundary condition and the strength of the endwall boundary layer. A simple force balance based on the centrifugal force near the endwall and the geostrophic pressure gradient defines a force imbalance that drives the endwall flow. Using this simple approach [Eq. (3)], the direction and relative strength of the boundary flow adjacent to the endwall can be predicted. Not only is this valuable for the cases presented here in which only the inner cylinder rotates, it could be applied to the much more complicated case where both cylinders rotate. As predicted from the force imbalance near the endwalls, the endwall flow is much stronger for the case of rotating endwalls than for fixed endwalls. Interestingly, for stress-free endwalls, the strength of the endwall flow is similar to that for rotating endwalls. Furthermore, computations of the stress-free endwall case show that it is possible to obtain either an inflow or an outflow, depending of the initial conditions for the computations.

The interaction between the endwall boundary layer and the Taylor vortex near the endwall results in endwall vortices that are asymmetric and axially elongated. The asymmetry is driven by the endwall boundary layer flow, so that the vortex has a higher velocity in the meridional plane near the inner cylinder for fixed endwalls and a higher velocity near the outer cylinder for rotating endwalls. In both cases, the endwall vortex is elongated by up to 30%. Both the asymmetry and the axial elongation disappear for the case of stress-free endwalls. In this case, the vortices near the endwalls are symmetric and have a square aspect ratio just like the Taylor vortices far from the endwalls.

The interaction between the endwall boundary condition and the centrifugal instability has a profound effect on the bifurcation phenomena. Near the endwall, the radial velocity smoothly increases with Reynolds number even well below the critical Reynolds number for no-slip endwalls due to the endwall vortices, which are unrelated to the Taylor centrifugal instability. Only in the case of a stress-free endwall does the radial velocity change sharply from zero to a finite value at the transitional Reynolds number.

ACKNOWLEDGMENTS

Thanks to the scientific committee of Centre National de la Recherche Scientifique (CNRS) computing center (IDRIS) for supporting this work and to Richard Kotarba for technical assistance. Much of this work was performed during a visit by R.M.L. to Laboratory MSNM at Université de la Méditerranée, funded by Direction Scientifique Sciences Pour l'Ingénieur (CNRS).

[1] R. J. Lingwood, "Absolute instability of the Ekman layer and related rotating flows," J. Fluid Mech. **331**, 405 (1997).
[2] K. A. Cliffe, J. J. Kobine, and T. Mullin, "The role of anomalous modes in Taylor–Couette flow," Proc. R. Soc. London, Ser. A **439**, 341 (1992).
[3] T. B. Benjamin, "Bifurcation phenomena in steady flows of a viscous fluid II: Experiments," Proc. R. Soc. London, Ser. A **359**, 27 (1978).
[4] T. B. Benjamin and T. Mullin, "Anomalous modes in the Taylor experiment," Proc. R. Soc. London, Ser. A **377**, 221 (1981).
[5] T. AlziaryDeRoquefort and G. Grillaud, "Computation of Taylor vortex flow by a transient implicit method," Comput. Fluids **6**, 259 (1978).
[6] G. Pfister and I. Rehberg, "Space-dependent order parameter in circular Couette flow transitions," Phys. Lett. A **83**, 19 (1981).
[7] G. Ahlers and D. S. Cannell, "Vortex-front propagation in rotating Couette–Taylor flow," Phys. Rev. Lett. **50**, 1583 (1983).
[8] M. Lücke, M. Mihelcic, and K. Wingerath, "Front propagation and pattern formation of Taylor vortices growing into unstable circular Couette flow," Phys. Rev. A **31**, 396 (1985).
[9] D.-C. Kuo and K. S. Ball, "Taylor–Couette flow with buoyancy: Onset of spiral flow," Phys. Fluids **9**, 2872 (1997).
[10] V. Sobolik, B. Izrar, R. Lusseyran, and S. Skali, "Interaction between the Ekman layer and the Couette–Taylor instability," Int. J. Heat Mass Transf. **43**, 4381 (2000).
[11] T. B. Benjamin, "Bifurcation phenomena in steady flows of a viscous fluid I: Theory," Proc. R. Soc. London, Ser. A **359**, 1 (1978).
[12] J. E. Burkhalter and E. L. Koschmieder, "Steady supercritical Taylor vortex flow," J. Fluid Mech. **58**, 547 (1973).
[13] Y. Takeda, K. Kobashi, and W. E. Fischer, "Observation of the transient

behaviour of Taylor vortex flow between rotating concentric cylinders after sudden start,'' Exp. Fluids **9**, 317 (1990).
[14]H. P. Greenspan, *The Theory of Rotating Fluids* (Cambridge University Press, London, 1969).
[15]J. A. Cole, ''Taylor-vortex instability and annulus-length effects,'' J. Fluid Mech. **75**, 1 (1976).
[16]K. A. Cliffe and T. Mullin, ''A numerical and experimental study of anomalous modes in the Taylor experiment,'' J. Fluid Mech. **153**, 243 (1985).
[17]A. Lorenzen and T. Mullin, ''Anomalous modes and finite-length effects in Taylor–Couette flow,'' Phys. Rev. A **31**, 3463 (1985).
[18]T. Mullin and C. Blohm, ''Bifurcation phenomena in a Taylor–Couette flow with asymmetric boundary conditions,'' Phys. Fluids **13**, 136 (2001).
[19]O. Czarny, E. Serre, P. Bontoux, and R. M. Lueptow, ''Spiral and wavy vortex flows in short counter-rotating Taylor–Couette cells,'' Theor. Comput. Fluid Dyn. **16**, 5 (2002).
[20]E. Serre, E. CrespoDelArco, and P. Bontoux, ''Annular and spiral patterns in flows between rotating and stationary discs,'' J. Fluid Mech. **434**, 65 (2001).
[21]J. M. Vanel, R. Peyret, and P. Bontoux, ''A pseudospectral solution of vorticity streamfunction equations using the influence matrix technique,'' in *Numerical Methods for Fluid Dynamics II*, edited by K. W. Morton and M. J. Baines (Clarendon, Oxford, 1986), pp. 463–475.
[22]I. Raspo, S. Hughes, E. Serre, A. Randriamampianina, and P. Bontoux, ''A spectral projection method for the simulation of complex three-dimensional rotating flows,'' Comput. Fluids **31**, 745 (2002).
[23]A. Recktenwald, M. Lücke, and H. W. Müller, ''Taylor vortex formation in axial through-flow: Linear and weakly nonlinear analysis,'' Phys. Rev. E **48**, 4444 (1993).
[24]H. A. Snyder and R. B. Lambert, ''Harmonic generation in Taylor vortices between rotating cylinders,'' J. Fluid Mech. **26**, 545 (1966).
[25]J. P. Gollub and M. H. Freilich, ''Optical heterodyne test of perturbation expansions for the Taylor instability,'' Phys. Fluids **19**, 618 (1976).
[26]T. Berland, T. Jøssang, and J. Feder, ''An experimental study of the connection between the hydrodynamic and phase-transition descriptions of the Couette–Taylor instability,'' Phys. Scr. **34**, 427 (1986).
[27]R. M. Heinrichs, D. S. Cannell, G. Ahlers, and M. Jefferson, ''Experimental test of the perturbation expansion for the Taylor instability at various wavenumbers,'' Phys. Fluids **31**, 250 (1988).
[28]S. T. Wereley and R. M. Lueptow, ''Azimuthal velocity in supercritical circular Couette flow,'' Exp. Fluids **18**, 1 (1994).
[29]S. T. Wereley and R. M. Lueptow, ''Spatio-temporal character of supercritical circular Couette flow,'' J. Fluid Mech. **364**, 59 (1998).
[30]S. J. Tavener, T. Mullin, and K. A. Cliffe, ''Novel bifurcation phenomena in a rotating annulus,'' J. Fluid Mech. **229**, 483 (1991).
[31]G. P. Neitzel, ''Numerical computation of time-dependent Taylor-vortex flows in finite-length geometries,'' J. Fluid Mech. **141**, 51 (1984).
[32]T. Mullin, ''Finite-dimensional dynamics in Taylor–Couette flow,'' IMA J. Appl. Math. **46**, 109 (1991).
[33]G. Pfister, H. Schmidt, K. A. Cliffe, and T. Mullin, ''Bifurcation phenomena in Taylor–Couette flow in a very short annulus,'' J. Fluid Mech. **191**, 1 (1988).